Universiteit Leiden
The Netherlands

The good? The bad? The mutant! Characterization of cancer-related somatic mutations and identification of a selectivity hotspot in adenosine receptor
Wang, X.

Chapter 7

Identification of V6.51L as a selectivity hotspot in stereoselective A$_{2B}$ adenosine receptor antagonist recognition.

Abstract

The four adenosine receptors (ARs) A_1AR, $A_{2A}AR$, $A_{2B}AR$, and A_3AR are G protein-coupled receptors (GPCRs) for which an exceptional amount of experimental and structural data is available. Still, limited success has been achieved in getting new chemical modulators on the market. As such, there is a clear interest in the design of novel selective chemical entities for this family of receptors. In this work, we investigate the selective recognition of ISAM-140, a recently reported $A_{2B}AR$ reference antagonist. A combination of semipreparative chiral HPLC, circular dichroism and X-ray crystallography was used to separate and unequivocally assign the configuration of each enantiomer. Subsequently affinity evaluation for both A_{2A} and A_{2B} receptors demonstrate the stereospecific and selective recognition of (*S*)-ISAM140 to the $A_{2B}AR$. The molecular modeling suggested that the structural determinants of this selectivity profile would be residue $V250^{6.51}$ in $A_{2B}AR$, which is a leucine in all other ARs including the closely related $A_{2A}AR$. This was herein confirmed by radioligand binding assays and rigorous free energy perturbation (FEP) calculations performed on the $L249^{6.51}V$ mutant $A_{2A}AR$ receptor. Taken together, this study provides further insights in the binding mode of these $A_{2B}AR$ antagonists, paving the way for future ligand optimization.

Introduction

Adenosine receptors (ARs) are a family of G protein-coupled receptors (GPCR) for which an exceptional amount of structural and experimental data is available[1,2]. Still, the number of therapeutic agents on the market that specifically target this family of receptors remains relatively low[3]. On the other hand, selectively targeting any of the four adenosine receptor subtypes (A$_1$, A$_{2A}$. A$_{2B}$ and A$_3$) provides an interesting avenue to address not only unmet therapeutic needs[4] and limited off-target effects[5], but also to help elucidating the (patho)physiological role of the different receptors within the family. One topic that is receiving increasing interest is the molecular mechanisms by which the two A$_2$AR subtypes regulate the immune response to tumor growth and metastasis[6].

Over the last years, different AR ligands have been developed with optimized selectivity profiles[7–9]. Within these AR ligand design programs, the generation of potent and selective antagonists has allowed the identification of powerful chemical tools to characterize each of the members of this receptor family. Examples include the A$_{2A}$AR selective antagonist ZM241385, and the A$_{2B}$AR selective antagonist ISAM-140, the latter originating from our in-house optimization program (Figure 1)[7,9–11]. The development of ISAM-140 was done following careful structure-affinity relationship (SAR) modeling, based on a computational binding mode of this chemotype, which suggested an important role of the stereogenic center in the heterocyclic scaffold in its high binding affinity (Figure 1)[7,11]. The prediction of the active stereoisomer for this chemotype was later confirmed indirectly by experimental characterization of the active stereoisomers for representative compounds of a series of cyanopyrimidines[10], fluorinated tricyclic derivatives[12] and aza-bioisosteres of the pentagonal heterocycle[13]. This binding model proposed that the stereospecific complementarity to the A$_{2B}$AR cavity was due to the optimal accommodation of the thiophene/furan ring around the chiral center of the core scaffold (Figure 1), with the A$_{2B}$AR specific residue V250[6.51] (Ballesteros Weinstein numbering in superscripts)[14]. Indeed, this valine is replaced by a leucine in all other AR subtypes, which could explain the highly selective profile of these series of non-planar antagonists towards the A$_{2B}$AR.
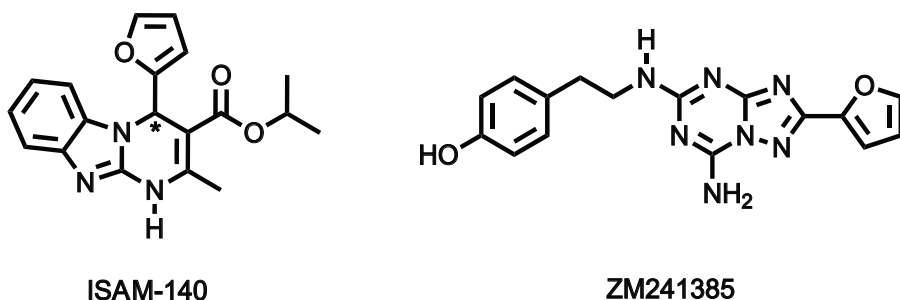

ISAM-140

ZM241385

Figure 1: 2D representation of the chemical structures of the AR ligands used in this work, i.e. ZM241385, (±) ISAM-140, (R)-ISAM-140 and (S)-ISAM-140. The chiral center in ISAM-140 is indicated with an asterisk.

In this work, we report the chiral separation of ISAM140 and confirm its stereospecific binding mode to the $A_{2B}AR$. An $A_{2A}AR$ construct was designed to include the corresponding $A_{2B}AR$ valine sidechain (L249V$^{6.51}$ $A_{2A}AR$ mutant), which in line with the starting hypothesis partially recovered the affinity for ISAM-140. Interestingly, this effect was observed for both stereoisomers of the antagonist, and is herein explained on the basis of structure-energetic modeling via rigorous free energy perturbation (FEP) calculations. These results validate the proposed role of V250$^{6.51}$ in the $A_{2B}AR$ subtype selectivity of these stereospecific chemotype, and paves the road for further design of selective antagonists as well as dual A_2AR ligands.

Methods

HPLC separation and characterization of ISAM-140 enantiomers

The chiral resolution was performed using a Water Breeze™ 2 (binary pump 1525, detector UV/Visible 2489, 7725i Manual Injector Kit 1500 Series). Compound ISAM-140 enantiomers were separated using a 250 mm x 20 mm Chiralpak® 5µm IE-3 (DAICEL) All the separations were performed at 25 ºC with hexane/isopropanol 7:3 as mobile phase. The enantiomers [(*R*)-ISAM-140 (3 mg, t_R = 17.90 min), (*S*)-ISAM-140 (3.1 mg, t_R = 20.31 min)] were isolated, their stereochemical purity analyzed by chiral HPLC (ee: 97-99% for each enantiomer) and then characterized by NMR.

Circular dichroism

Circular dichroism spectra were recorded on a Jasco-815 system equipped with a Peltier-type thermostatic accessory (CDF-426S, Jasco). Measurements were carried out at 20 °C using a 1 mm quartz cell in a volume of 600 µL. Compounds (0.5 mg) were dissolved in MeOH (1.0 mL) and then diluted 10-fld in MeOH. The instrument settings were bandwidth, 1.0 nm; data pitch, 1.0 nm; speed, 500 nm/min; accumulation, 10; wavelengths, 400−190 nm.

X-ray crystallography of ISAM-140 enantiomers

Crystals of (*S*)-ISAM-140 and (*R*)-ISAM-140 were grown by slow evaporation from ethanol solutions. For the crystal structure determination, the data were collected by applying the omega and phi scans method on a Bruker D8 VENTURE PHOTON III-14 diffractometer using Incoatec multilayer mirror monochromated with Cu-Kα radiation (λ = 1.54178 Å) from a microfocus sealed tube source at 100 K with detector resolution of 7.3910 pixels mm-1. Computing data and reduction were made with the APEX3 v2018.7-2 (BRUKER AXS, 2005). The structure was solved using SHELXT2018/22 and finally refined by full-matrix least-squares based on F2 by SHELXL2018/3.3 An empirical absorption correction was applied using the SADABS2016/2 program. Software used to molecular graphics: ORTEP for Windows. Software used to prepare material for publication: WinGX2018.3 publication routines4 and Mercury.

The obtained structures were refined as follows: All non-hydrogen atoms were refined anisotropically and the hydrogen atom positions were included in the model on the basis of Fourier difference electron density maps. All aromatic CH hydrogen (C-H = 0.95 Å), methine hydrogen (C-H = 1.0 Å) and methylene hydrogen (C-H=0.99 Å) atoms were refined using a riding model with Uiso(H) = 1.2 Ueq(C). The methyl hydrogen (C-H = 0.98 Å) atoms were refined as a rigid group with torsional freedom [Uiso(H) = 1.5 Ueq(C)] and the hydrogens atom of NH groups (HiN) as a free atom with Uiso(H) = 1.2 Ueq(C).

Site-directed mutagenesis

Site-directed mutants of the A$_{2A}$AR were generated by polymerase chain reaction (PCR) mutagenesis as described previously[15]. pcDNA3.1(+)-hA$_{2A}$AR with N-terminal HA and FLAG tags and a C-terminal His tag was used as the template. Primers for mutants L249V[6.51] and L249A[6.51] were designed by the QuikChange Primer Design Program of Agilent Technologies (Santa Clara, CA, USA) and primers were obtained from Eurogentec (Maastricht, The Netherlands). All DNA sequences were verified by Sanger sequencing at LGTC (Leiden, The Netherlands).

Cell culture and transient transfection

CHO cells stably expressing the human A$_{2B}$AR (CHO-spap-hA$_{2B}$AR) were cultured in Dulbecco's modified Eagle's medium: Nutrient Mixture F-12 (DMEM/F12) supplemented with 10% newborn calf serum, 50 µg/mL streptomycin, and 50 IU/mL penicillin at 37°C and 5% CO$_2$ atmosphere. Cells were subcultured twice a week at a confluency of 80 - 90%. For transient transfections, human embryonic kidney (HEK) 293 cells were cultured as monolayers in DMEM supplemented with stable glutamine, 10% newborn calf serum, 50 µg/mL streptomycin, and 50 IU/mL penicillin at 37°C and 7% CO$_2$ atmosphere as reported previously[15,16]. The cells were seeded on 10 cm ø plates and transfected with 10 µg plasmid DNA of wild-type (WT) or mutant hA$_{2A}$AR using the calcium phosphate precipitation method[17], followed by a 48-hour incubation.

Membrane preparation

HEK293 cells transiently expressing WT or mutant human A$_{2A}$AR (HEK293-hA$_{2A}$AR) were detached from the plates 48 h post-transfection by scraping into phosphate-buffered saline (PBS) and collected by centrifugation at 1,000 × g for 5 minutes. The pellets from 10 plates were pooled and resuspended in ice-cold Tris-HCl buffer (50 mM, pH 7.4) and then homogenized with an UltraTurrax homogenizer (Heidolph Instruments, Schwabach, Germany). The cell membrane suspensions were centrifuged at 100,000 × g at 4°C for 20 minutes in a Beckman Optima LE-80K ultracentrifuge. The pellet was resuspended in ice-cold Tris-HCl buffer, and the homogenization and centrifugation steps were repeated one more time. After this, Tris-HCl buffer was used to resuspend the pellet of HEK293 cell membranes. Membrane preparation for CHO-spap-hA$_{2B}$AR cells followed a similar procedure after

they were grown to 90% confluence in 15 cm plates, and membranes pellets were finally resuspended in Tris-HCL buffer containing 10 % (w/v) CHAPS. In both cases, 0.8 IU/ml adenosine deaminase was added to break down endogenous adenosine and membranes were aliquoted into 250 μL and stored at -80°C until further use. Membrane protein concentrations were determined using the BCA method[18].

Radioligand binding assays

Radioligand binding experiments on CHO-spap-hA$_{2B}$AR membranes were adjusted from previously reported data[19]. Membrane aliquots containing 30 μg of protein were incubated in a total volume of 100 μL of assay buffer. Nonspecific binding was determined with 10 μM ZM241385. Then 25 μL cell membrane suspension, 25 μL of 1.5 nM radioligand [^{3}H]PSB-603, 25 μL of assay buffer [50 mM Tris-HCl, 0.1 % (w/v) CHAPS, pH 7.4 at 25°C] and 25 μL of the indicated compounds in increasing concentrations in the same assay buffer were added to each well and followed by a 120 min incubation at 25 °C. Radioligand displacement experiments with transient HEK293-hA$_{2A}$AR cell membranes were performed as described previously[20]. Briefly, membrane aliquots containing 5-7.5 μg of protein were incubated in a total volume of 100 μL of assay buffer to adjust the assay window to approximately 2000 DPM. Nonspecific binding was determined in the presence of 100 μM NECA and represented less than 10% of the total binding. Then 25 μL membrane suspension (5-7.5 μg of protein), 25 μL of 5.0 nM radioligand [^{3}H]ZM241385, 25 μL of assay buffer [50 mM Tris-HCl, pH 7.4] and 25 μL of the indicated compounds at different concentrations in the same assay buffer were added to each well, with final assay concentration of radioligand of 5 nM. For homologous displacement experiments, radioligand displacement experiments were performed with the presence of three concentrations of [^{3}H]ZM241385 (1.7 nM, 5.0 nM and 9.5 nM) and increasing concentrations of unlabeled ZM241385. After 120 minutes at 25°C, incubations were terminated by rapid vacuum filtration through GF/B filter plates (PerkinElmer, Groningen, Netherlands) using a Perkin Elmer Filtermate-harvester. Filterplates were subsequently washed ten times with ice-cold assay buffer. Filter-bound radioactivity was determined by scintillation spectrometry using a Microbeta$^{2®}$ 2450 microplate counter (PerkinElmer).

Data analysis

Data analyses were performed using GraphPad Prism 7.0 software (GraphPad Software Inc., San Diego, CA). pK$_D$ values and B$_{max}$ were obtained by non-linear regression analysis using "one-site homologous" model. pIC$_{50}$ values were determined by fitting the data using non-linear regression to a sigmoidal concentration-response curve equation. pK$_i$ values were calculated from pIC$_{50}$ values using the Cheng-Prusoff equation[21].

Computational Modeling

The high resolution crystal structure of the A$_{2A}$AR (PDB code 4EIY[22]) was used as

a starting point for the calculations. The protein was prepared for MD simulations as follows: (i) removing co-factors and fused proteins employed for crystallization, (ii) reverting the crystal construct to the wild-type (WT) A$_{2A}$AR receptor, (iii) the assignment of protonation states of ionizable residues. (iv) mutation of the WT Leu249$^{6.51}$ to Val as in the corresponding A$_{2B}$AR and (v) membrane insertion using PyMemDyn[23]. The latter stage involves embedding of the protein in a pre-equilibrated POPC membrane, soaking of the system with bulk water and a short (5 ns) equilibration period with GROMACS 4.6.[24] using the OPLS-AA force field[25] and Berger parameters for the lipids[26]. Thereafter, ligands were manually docked to the equilibrated receptor using as a reference the putative binding mode of SYAF014[7] to the A$_{2B}$AR previously described. In the case of ZM241385, the coordinates of the crystal structure ligand were retained during the equilibration process. Subsequently, each equilibrated L249$^{6.51}$V-A$_{2A}$AR-ligand complex was transferred to the MD software Q[27] for free energy perturbation (FEP) calculations under spherical boundary conditions using QligFEP[28]. A 25Å sphere centered on the center of geometry of the ligand was constructed for these MD simulations. Solvent atoms were subject to polarization and radial restraints using the surface-constrained all-atom solvent (SCAAS)[29] model to mimic the properties of bulk water at the sphere surface. Atoms lying outside the simulation sphere were tightly constrained (200 kcal/mol/Å^2 force constant) and excluded from the calculation of non-bonded interactions. Long range electrostatic interactions beyond a 10 Å cut off were treated with the local reaction field method[30], except for the atoms undergoing the FEP transformation, where no cutoff was applied. Solvent bond and angles were constrained using the SHAKE algorithm[31]. All titratable residues outside the sphere were neutralized as reported elsewhere[28]. Residue parameters were translated from the OPLS-AA/M force field[32] and the parameters for the ligand and lipids were inherited from the previous MD stage. The simulation sphere was warmed up from 0.1 to 298 K, during a first equilibration period of 0.61 nanoseconds, where an initial restraint of 25 kcal/mol/Å^2 imposed on all heavy atoms was slowly released for all complexes. Thereafter the system was subject to 10 parallel replica MD simulations, in which the FEP protocol was applied for each residue transformation. Each of these MD replicates started with a 0.25 nanosecond unbiased equilibration period, with different initial velocities. The FEP protocol for the L $\rightarrow$ V mutation was generated by combing the QresFEP[33] protocol for residue mutations with a dual topology approach inspired from QligFEP[28], where the effective topology along the transformation is a linear combination of the two original sidechain topologies. Each FEP transformation consisted of 51 evenly distributed λ-windows with 10 ps MD sampling each. In order to fulfill a thermodynamic cycle and calculate relative binding free energies, parallel FEP transformations were run for the apo-structure, i.e. the protein structure without ligand. In these simulations the same parameters were applied (i.e., sphere size, simulation time, etc.), and a total of 10 replicates x 2 (apo/holo) states x 2 (WT and mut) annihilations x 51 λ-windows x 10 ps = 20.4 ns sampling was performed for each mutation simulation. The relative binding free energy shift between WT and mutant receptors for each ligand was estimated by solving the thermodynamic

cycle utilizing the Bennett acceptance ratio (BAR)[34]. All 3D images were produced in PyMOL[44].

Results

Generating A_{2A}AR-ligand models

The binding mode of (*S*)-ISAM-140 was obtained by superposition of the previously published complex of this molecule with our A_{2B}AR homology-based model[11] onto a modeled L249$^{6.51}$V A_{2A}AR mutant, i.e. introducing the A_{2B}AR sidechain in this position. Such a construct was built and equilibrated on the basis of the high-resolution crystal structure of the ZM241385 — A_{2A}AR complex (see *Methods*)[22]. The binding mode obtained included the two key interactions typical of ARs antagonists: (i) hydrogen bond(s) with N253$^{6.55}$ and (ii) π–π stacking with F168^{EL2}, both residues completely conserved among ARs[1]. The high-affinity A_{2A}AR antagonist ZM241385 showed an optimal shape complementarity with the A_{2A}AR WT residue L249$^{6.51}$ (Figure 2A), whereas the corresponding L249V$^{6.51}$ mutant is expected to minimally disrupt this shape complementarity due to a reduced volume (Figure 2B). On the other hand, the obtained binding modes for (*S*)-ISAM-140 on the WT A_{2A}AR (also obtained assuming the same binding mode as in the A_{2B}AR homology-based model[11]) showed a non-optimal fit, in accordance with the lack of affinity exhibited for the A_{2A}AR receptor by this derivative and other compounds within the series[8–11]. In particular, the presence of the native L249$^{6.51}$ in the A_{2A}AR appeared to introduce a steric clash with either the 2-furyl or 3-thienyl substituents of the ligands, which we hypothesized would reduce binding affinities (Figure 2C). Conversely, introducing the A_{2B}AR sidechain on the modeled L249V$^{6.51}$ A_{2A}AR mutant provided a better shape complementarity (Figure 2D), allowing us to hypothesize that the binding affinity of these antagonists might be recovered to some extent.

Chiral separation of ISAM-140

The racemic mixture of ISAM-140, obtained as previously described,[11] was resolved into its enantiopure forms. A combination of chiral HPLC, circular dichroism (CD) spectroscopy and X-ray crystallography was employed to separate and unequivocally assign the configuration of the heterocyclic stereocenter in each stereoisomer. Semipreparative HPLC separation of (±) ISAM-140 on a chiral stationary phase (see *Experimental information*) provided the expected enantiomers (Figure 3) with excellent stereochemical purity (> 97%). As described previously for 3,4-dihydropyrimidin-2-ones[35–37], the characteristic CD activity of the enamide chromophore (300–350 nm) allowed the unambiguous assignment of the absolute configuration of each enantiomer (Figure 3) by comparison with the reported CD data for enantiopure 3,4-dihydropyrimidin-2(1*H*)-ones of known configuration. In the structures shown in Figure 3, enantiomers that show a negative Cotton effect (red line) contain the furan ring pointing backwards, which corresponds to (*S*)-ISAM-140.

In contrast, the stereoisomers giving a positive Cotton effect (blue line) contain the pentagonal heterocycle pointing forward, which corresponds to (*R*)-ISAM-140. Single crystals suitable for X-ray analysis were grown by slow evaporation of each enantiomer in ethanol. The structures were solved and the data extracted form X-ray crystallography of both monocrystals presented in the Supporting Information (Supplementary Table S1)[12]. The crystal structures of (*S*)-ISAM-140 and (*R*)-ISAM-140 (monoclinic, Figure 3) confirmed the configuration assignment established by circular dichroism. The benzimidazole moiety is essentially planar in both enantiomers, while the dihydropyrimidine core adopt a pseudo envelope conformation, with the C$_4$ atom being lightly displaced by 0.26Å.
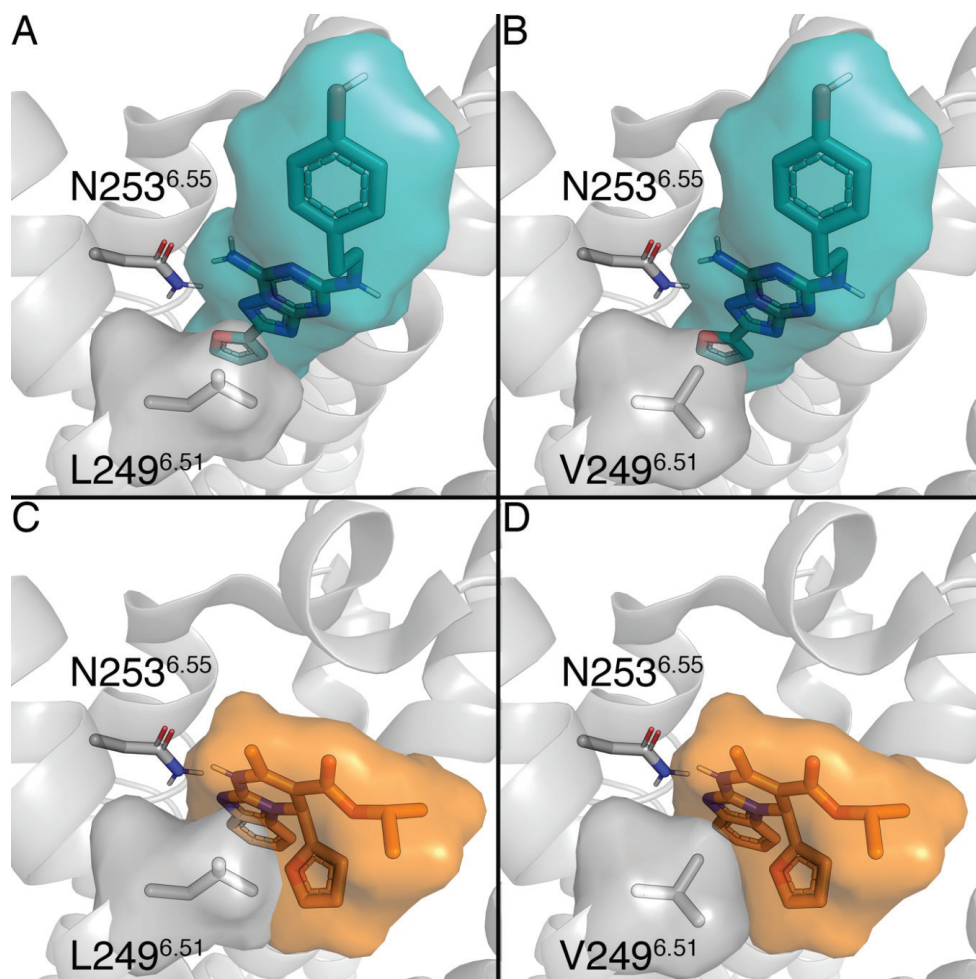

Figure 2: Binding mode of two ligands, ZM241385 (in blue, panels A and B) and (*S*)-ISAM-140 (orange, panels C and D), to the WT (panels A and C) and the L249V[6.51] mutant (panels B and D) A$_{2A}$AR. Volumetric occupancies are shown as surface. Figure created with Pymol v2.0.
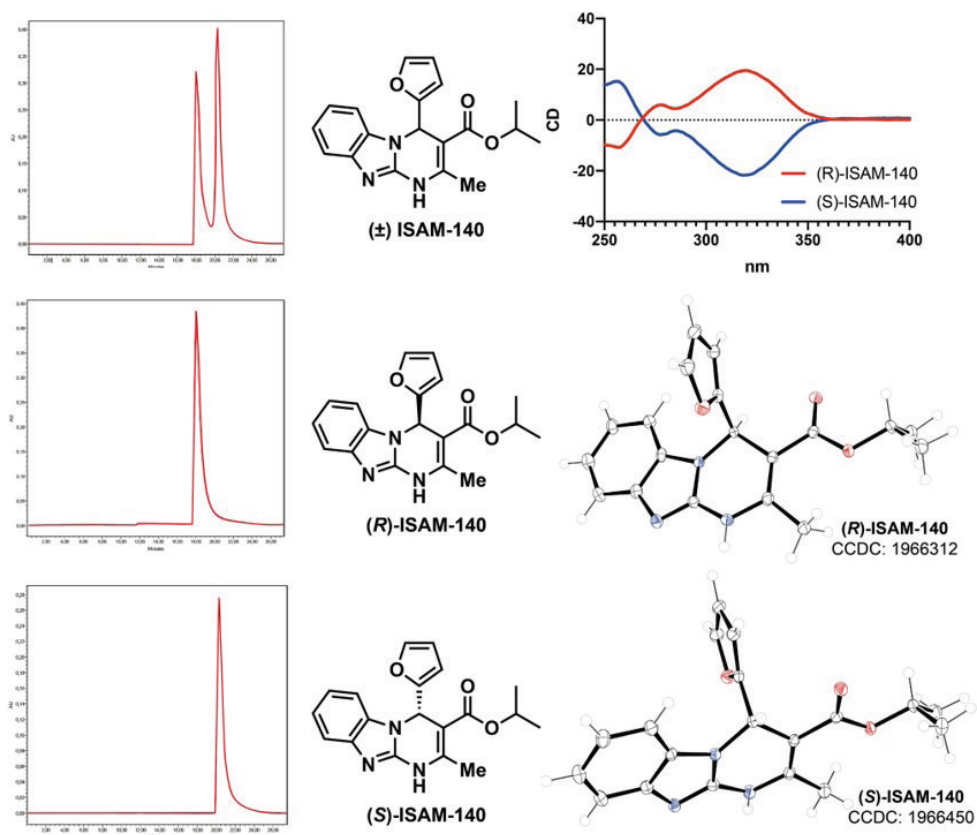
Figure 3. Chiral HPLC separation, circular dichroism spectra and crystal X-ray structure of compounds (R)-ISAM-140 and (S)-ISAM-140.

Determination of ligand binding affinities

To further confirm the role of position 6.51 as a receptor selectivity hotspot, we attempted to express L249V/A$^{6.51}$ A$_{2A}$AR and V250L/A$^{6.51}$ A$_{2B}$AR mutant receptors. Whilst both A$_{2A}$AR mutant receptors were successfully expressed (Supplementary Fig. S1), none of the A$_{2B}$AR mutants could be expressed using standard (non-viral) transfection methods, and consequently the A$_{2B}$AR mutants designed had to be excluded from further experimentation. Thereafter, we determined the binding affinity of ISAM-140, both as a racemate and pure enantiomers, together with the prototypical antagonist ZM241385 at both WT and mutant A$_{2A}$ARs, as well as at the WT A$_{2B}$AR (Figure 4 and Table 1). The affinities determined for ZM241385 and racemic ISAM-140 on WT A$_{2B}$AR (pKi of 6.78 and 7.86, respectively, see Table 1) were in line with previous reports[10]. As expected from the modeling, the corresponding data for the enantiopure forms of ISAM-140 showed that the affinity of the racemic mixture was due to (S)-ISAM-140, with even a gain in binding affinity as compared to the racemic mixture (ΔpK$_i$ = 0.19), which was dramatically reduced for the low-affinity

(R)-ISAM-140 (ΔpK$_i$ = 1.31 between both enantiomers, Figure 4A and Table 1).

For the A$_{2A}$AR, we first established whether the L249V/A$^{6.51}$ mutants still sufficiently bound ZM241385, to validate the viability of using it as a radioligand in the homologous displacement assays. Of note, the resulting K$_D$ values could then be used to obtain K$_i$ values from the IC$_{50}$ values (see *Methods*), which enabled us to compare affinity values for WT and mutant A$_{2A}$ARs. Moreover, the resulting B$_{max}$ values showed that the A$_{2A}$AR L249V$^{6.51}$ mutant had a lower expression level than compare affinity values for WT and mutant A$_{2A}$ARs. Moreover, the resulting B$_{max}$ values showed that the A$_{2A}$AR L249V$^{6.51}$ mutant had a lower expression level than the WT A$_{2A}$AR. A slight reduction in affinity of both [^{3}H]ZM241385 and ZM241385 was observed on this mutant (Table 1), which was in line with our hypothesis that the shape complementarity between ZM241385 and L249 is mostly preserved with
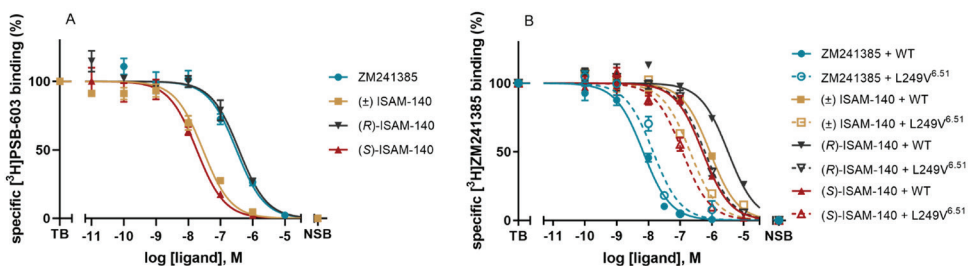
Figure 4: Displacement of (A) specific [^{3}H]PSB-603 binding from A$_{2B}$AR and (B) specific [^{3}H]ZM241385 binding from the WT and the L249V$^{6.51}$ mutant A$_{2A}$AR at 25 °C by ZM241385 (blue), (±) ISAM-140 (yellow), (R)-ISAM-140 (black) and (S)-ISAM-140 (red). Combined graphs are from three individual experiments performed in duplicate.
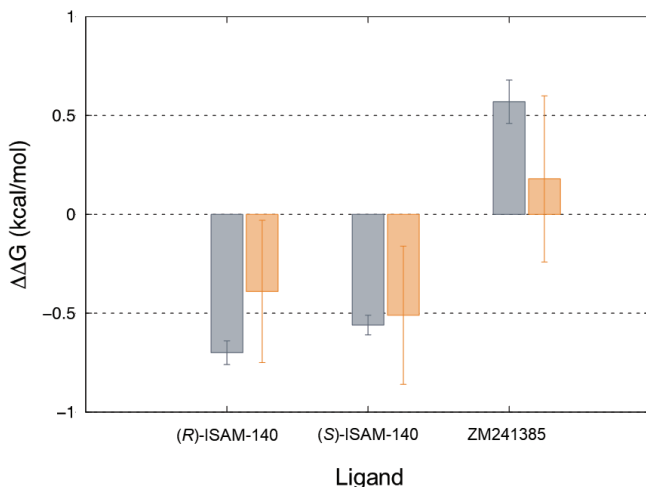
Figure 5: Experimental (grey) and calculated (orange) relative changes in binding free energies to the L249V$^{6.51}$ mutant A$_{2A}$AR for the two enantiomers of ISAM-140 and ZM241385.

Table 1: B_{max} and pK_D values of [^{3}H]ZM241385 and binding affinities of ZM241385, (±) ISAM-140, (R)-ISAM-140 and (S)-ISAM-140 on WT A_{2B}AR, WT and L249V[6.51] mutant A_{2A}ARs.

Receptor	B_{max} (pmol/mg) [a]	pK_D [a]	pK_i [b]			
	[^{3}H]ZM241385	ZM241385	ZM241385	(±) ISAM-140	(R)-ISAM-140	(S)-ISAM-140
A_{2B}AR (WT)	-	-	6.78 ± 0.06	7.86 ± 0.09	6.74 ± 0.09	8.05 ± 0.06
A_{2A}AR (WT)	3.92 ± 0.23	8.59 ± 0.09	8.62 ± 0.04	6.53 ± 0.03	5.96 ± 0.02	6.76 ± 0.04
A_{2A}AR (L249V)	1.15 ± 0.15	8.17 ± 0.06	8.09 ± 0.03	6.92 ± 0.03	6.47 ± 0.07	7.17 ± 0.09

Data is presented as mean ± SEM of three individual experiments, each performed in duplicate.
[a] B_{max} and pK_D values obtained from homologous competition displacement assays on transiently transfected HEK293-A_{2A}AR membranes at 25 °C.
[b] pK_i values obtained from displacement assays of specific [^{3}H]PSB-603 binding from CHO-spap-hA_{2B}AR membrane or specific [^{3}H]ZM241385 binding from transiently transfected WT and mutant HEK293-A_{2A}AR membranes at 25 °C.

a smaller Val. However, a substantial hydrophobic side chain was important for the binding of this antagonist to the A_{2A}Rs, since its affinity to the A_{2A}AR L249A[6.51] mutant was completely lost (Supplementary Figure. S2), in line with previous reports[38]. The results of the displacement assays for ISAM-140 (racemate and both stereoisomers) are illustrated in Figure 4B and Table 1. Although one data point for (±) ISAM-140 at the concentration of 10^{-5} M was excluded from the curve of WT A_{2A}AR, due to low water solubility, in all cases the binding affinity for the WT A_{2A}AR was very low (within micromolar range). Notably, it followed the same trend as observed on WT A_{2B}AR, i.e. the highest affinity for (S)-ISAM-140 and the lowest for (R)-ISAM-140. The selectivity ratio between A_{2B} and A_{2A} ARs was substantial for (±) ISAM-140, (ΔpK_i = 1.33), in line with the previous reports for this ligand[11]. This difference that was maintained for the active eutomer (S)-ISAM-140 (ΔpK_i = 1.29) and, to a lower extent, even for (R)-ISAM-140 (ΔpK_i = 0.79), which is expected due to its already low affinity for A_{2B}AR. Notably, the affinity values were significantly recovered at the A_{2A}AR L249A[6.51] mutant, i.e. when the receptor was more "A_{2B}AR-like", thus supporting the initial modeling hypothesis. The moderate affinity gains observed for the A_{2A}AR L249A[6.51] mutant as compared to the A_{2A}AR WT (0.39, 0.41 and 0.51 log unit for (±) ISAM-140, (S)-ISAM-140, and (R)-ISAM-140, respectively, see Table 1) did not restore the affinity values as in the WT A_{2B}AR.

Computational characterization of binding free energies.

Finally, we investigated the observed shifts in binding affinities for (S)-ISAM-140, (R)-ISAM-140 and ZM241385 in the context of the structural binding model of these molecules to the A_{2A}AR. The approach was to compare the WT and L249[6.51]V mutant (A_{2B} equivalent) versions of A_{2A}AR using the Q-FEP protocols[28,33]. This strategy consists on the simulation of the mutation (Leu to Val) both in the presence and absence of each of the docked ligands. While the structure of the ZM241385 — A_{2A}AR complex is experimentally known[22], the binding mode of each enantiomer

of ISAM140 was inferred from our previous work on this chemotype[7]. Figure 5 summarizes the calculated shift in the free energy of binding due to the L249[6.51]V mutation for each enantiomer of ISAM-140 and for ZM241385. It can be observed a very good agreement between the calculations and the experimental affinity data here reported in Figure 4B, with a very low mean average error (MAE=0.25 kcal/mol, numerical data provided in Supplementary Table S2). Thus, the simulation of this mutation resulted in a predicted increase in affinity (negative $\Delta\Delta G_{bind\ (mut\ -\ WT)}$ values in Figure 5) for both enantiomers of ISAM-140, with values proportional to those extracted from the experimental data. Conversely, the experimental affinity of ZM241385 is decreased for the L249[6.51]V mutant $A_{2A}AR$, which is also captured by our modeling as a mild positive value for the calculated $\Delta\Delta G_{bind\ (mut\ -\ WT)}$.

Discussion

In this work, we investigated the role of position 6.51 in determining the specificity for $A_{2B}AR$ binding of a series of chiral antagonists recently developed for this receptor. The modeling hypothesis behind the design of the potent antagonist ISAM-140 placed the *S*-stereoisomer in perfect shape complementarity with Val250[6.51] in the $A_{2B}AR$, while analogous docking in the high resolution $A_{2A}AR$ bearing a bulkier Leu in the same position showed initial steric clashes. This allowed us to propose this sidechain as a landmark for $A_{2B}AR$ selectivity for this ligand class, and the (*S*)-ISAM-140 as the active stereoisomer. To experimentally validate this hypothesis, the ISAM-140 enantiomers were separated and their absolute configuration unequivocally assigned. Besides this goal, the enantiomeric separation and pharmacological characterization of this reference $A_{2B}AR$ antagonist allowed to confirm the expected higher affinity of the *S* enantiomer, in line with the original modeling hypothesis[11] and recent similar results obtained with derivatives of this scaffold[10,12,13].

Site-directed mutagenesis of position 6.51 was performed on the $A_{2A}AR$ to replace the WT Leu by the Val specific of $A_{2B}AR$, as the reverse mutation of the $A_{2B}AR$ appeared unfeasible in our hands, somehow in contrast to previous report of Müller and co-workers who managed to express the corresponding Ala mutant (V250A[6.51]) in the $A_{2B}AR$[39]. It is worth noting that, while there had been reports of the Alanine scan of position 6.51 in both A_{2A}[38] and $A_{2B}ARs$[39], this is the first time that the introduction of the $A_{2B}AR$ characteristic Val sidechain on the $A_{2A}AR$ is evaluated.

The L249[6.51]V $A_{2A}AR$ mutant partially recovered the affinity of ISAM-140 lost for this receptor, supporting the initial modeling hypothesis. This partial recovery in affinity, consistently observed for all three forms of this molecule (i.e., racemic mixture and both eutomers) is in line with recent reports on 'selectivity hotspots' between A_1AR and $A_{2A}AR$, where a single-point mutation clearly affecting the experimental binding mode could only partially explain the observed selectivity profile of the A_1AR selective xanthines under investigation[40]. On the other hand, the opposed effect was observed

7

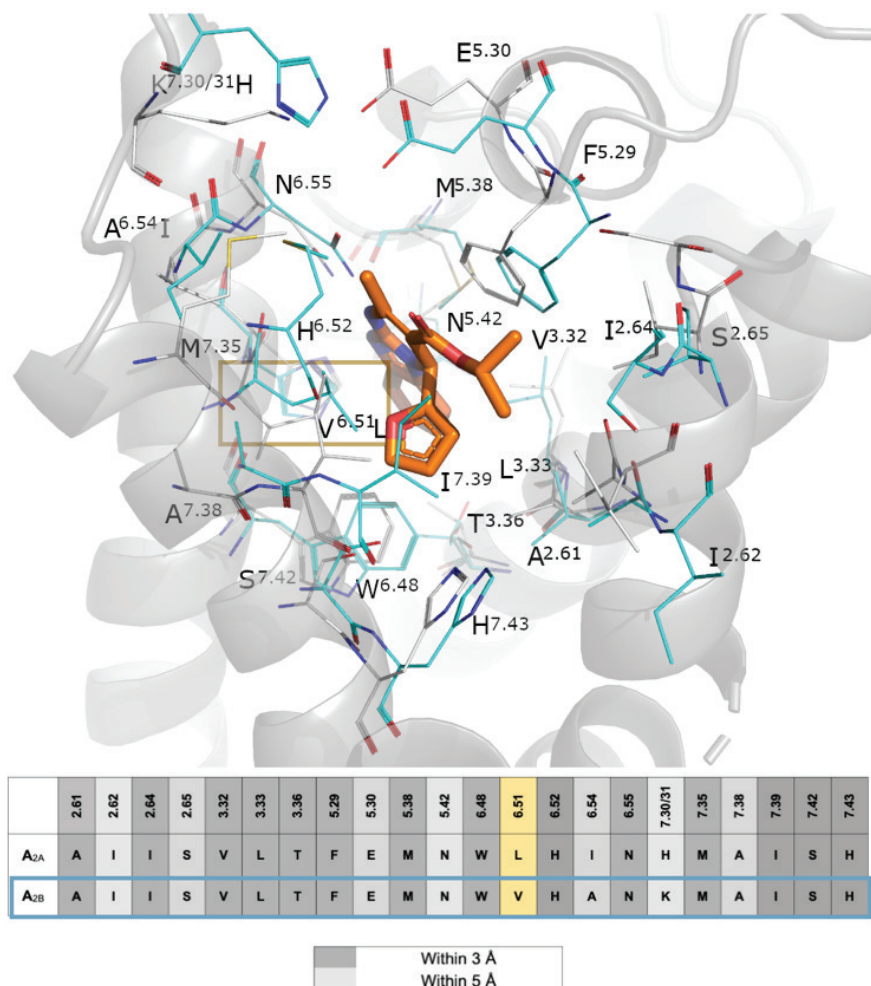|	2.61	2.62	2.64	2.65	3.32	3.33	3.36	5.29	5.30	5.38	5.42	6.48	6.51	6.52	6.54	6.55	7.30/31	7.35	7.38	7.39	7.42	7.43
A2A	A	I	I	S	V	L	T	F	E	M	N	W	L	H	I	N	H	M	A	I	S	H
A2B	A	I	I	S	V	L	T	F	E	M	N	W	V	H	A	N	K	M	A	I	S	H

Within 3 Å
Within 5 Å

Figure 6: Pseudo-sequence alignment of the residues within 5 Å of any atom of *(S)*-ISAM140, as predicted by docking on the $A_{2B}AR$, between this receptor and the $A_{2A}AR$. The location of each sidechain is shown in the 3D superposition of the *(S)*-ISAM140-$A_{2B}AR$ (gray sidechains and cartoon, ligand in orange sticks) with the $A_{2A}AR$ crystal structure (cyan sidechains). Position 6.51 is highlighted on a yellow box. Figure created with Pymol v2.0.

for ZM241385 (i.e. decrease in affinity for the L249$^{6.51}$V $A_{2A}AR$ mutant) in line with the well-described preference of this ligand for the $A_{2A}AR$.

To further assess the amino acid conservation between the A_{2A} and $A_{2B}ARs$ binding sites, a pseudo-sequence alignment is presented in Figure 6. One can observe that, in addition to position 6.51 here studied, only two sidechains vary within the 5Å cut-off distance with the ligand: Ala253$^{6.54}$ in $A_{2B}AR$, situated one helix turn below position 6.51, is an Ile in $A_{2A}AR$. This residue, however, is not in contact with the ligand and instead involved in the TM packing as shown in the Fig. 6. In the EL3 region, His264$^{7.31}$ in $A_{2A}AR$ is making a salt bridge interaction with Glu169$^{5.30}$ in EL2,

a role that in our A$_{2B}$AR model is undertaken by Lys267[7.31] (Figure. 6). While this residue has been shown to be involved in ligand binding kinetics[1], we should not rule out an additional role of the more variable EL regions in the selectivity profile of this antagonist. This analysis also allows to explore potential indirect effects of the V6.51L mutation on neighbouring residues conserved in the ARs, like His[6.52] that has been shown to be involved in both agonist and antagonist binding[1]. As it can be seen in Fig 6., this residue is not predicted to change conformation between A$_{2A}$ and A$_{2B}$ARs, which is supported by the water-mediated interaction with Asn[5.42] previously characterized by MD simulations of this pair of receptors[23].

In the lack of a crystal structure of the A$_{2B}$AR, the observed effects were rationalized back in the modeled structures, by means of first-principle FEP simulations of this mutation. The QresFEP protocol has been broadly applied to investigate the A$_{2A}$AR mutational landscape[41–43], showing exceptional sensitivity to capture the correct affinity shifts for different chemotypes. The binding model of *(S)*-ISAM-140 to the WT and L249[6.51]V mutant versions of A$_{2A}$AR was here assumed to be the same as our docking model of this compound to the WT A$_{2B}$AR[12]. That model suggested that the high A$_{2B}$AR affinity of (±) ISAM-140 was due to the stereoselective optimal fitting of the (*S*) isomer to the A$_{2B}$AR binding site, facilitated by the Val sidechain in position 6.51 of this receptor[12]. The calculated recovery of the binding affinity of *(S)*-ISAM-140 upon the L249[6.51]V mutation in the A$_{2A}$AR, which is in line with the experimental design of this A$_{2B}$-like mutation on the A$_{2A}$AR, further confirms the validity of the binding model for this chemotype on the A$_{2B}$AR.

Overall, both experimental and computational results of this study clearly support the binding mode used to design this study, providing useful structural insights in the selective recognition of these A$_{2B}$AR antagonists that should aid in future structure-based optimization.

7

References

1. Jespers, W. *et al.* Structural mapping of adenosine receptor mutations: ligand binding and signaling mechanisms. *Trends Pharmacol. Sci.* **39**, 75–89 (2017).
2. Jazayeri, A., Andrews, S. P. & Marshall, F. H. Structurally enabled discovery of adenosine A$_{2A}$ receptor antagonists. *Chem. Rev.* **117**, 21–37 (2017).
3. Gessi, S., Merighi, S. & Varani, K. Adenosine receptors: the status of the art. in *The Adenosine Receptors* **34**, 1–11 (2018).
4. Jacobson, K. A. & Gao, Z.-G. Adenosine receptors as therapeutic targets. *Nat. Rev. Drug Discov.* **5**, 247–264 (2006).
5. Chen, J.-F., Eltzschig, H. K. & Fredholm, B. B. Adenosine receptors as drug targets — what are the challenges? *Nat. Rev. Drug Discov.* **12**, 265–286 (2013).
6. Pardoll, D. M. The blockade of immune checkpoints in cancer immunotherapy. *Nature Reviews Cancer* **12**, 252–264 (2012).
7. Crespo, A. *et al.* Discovery of 3,4-dihydropyrimidin-2(1H)-ones as a novel class of potent and selective A$_{2B}$ adenosine receptor antagonists. *ACS Med. Chem. Lett.* **4**, 1031–1036 (2013).
8. Yaziji, V. *et al.* Pyrimidine derivatives as potent and selective A$_3$ adenosine receptor antagonists. *J. Med. Chem.* **54**, 457–471 (2011).
9. Jespers, W. *et al.* Structure-based design of potent and selective ligands at the four adenosine receptors. *Molecules* **22**, 1945 (2017).
10. Carbajales, C. *et al.* Enantiospecific recognition at the A$_{2B}$ adenosine receptor by alkyl 2-cyanoimino-4-substituted-6-methyl-1,2,3,4-tetrahydropyrimidine-5-carboxylates. *J. Med. Chem.* **60**, 3372–3382 (2017).
11. El Maatougui, A. *et al.* Discovery of potent and highly selective A$_{2B}$ adenosine receptor antagonist chemotypes. *J. Med. Chem.* **59**, 1967–1983 (2016).
12. Mallo-Abreu, A. *et al.* Trifluorinated pyrimidine-based A$_{2B}$ antagonists: optimization and evidence of stereospecific

recognition. *J. Med. Chem.* **62**, 9315–9330 (2019).

13. Mallo-Abreu, A. *et al.* Nitrogen-Walk Approach to Explore Bioisosteric Replacements in a Series of Potent A_{2B} Adenosine Receptor Antagonists. *J. Med. Chem.* **63**, 7721–7739 (2020).

14. Ballesteros, J. A. & Weinstein, H. Integrated methods for the construction of three-dimensional models and computational probing of structure-function relations in G protein-coupled receptors. in *Methods in Neurosciences* **25**, 366–428 (1995).

15. Guo, D. *et al.* Molecular basis of ligand dissociation from the adenosine A_{2A} receptor. *Mol. Pharmacol.* **89**, 485–491 (2016).

16. Guo, D., Mulder-Krieger, T., IJzerman, A. P. & Heitman, L. H. Functional efficacy of adenosine A_{2A} receptor agonists is positively correlated to their receptor residence time. *Br. J. Pharmacol.* **166**, 1846–1859 (2012).

17. Dasgupta, S. *et al.* Adenosine A_{2A} receptors modulate the binding characteristics of dopamine D_2 receptors in stably cotransfected fibroblast cells. *Eur. J. Pharmacol.* **316**, 325–331 (1996).

18. Smith, P. K. *et al.* Measurement of protein using bicinchoninic acid. *Anal. Biochem.* **150**, 76–85 (1985).

19. Schiedel, A. C. *et al.* The four cysteine residues in the second extracellular loop of the human adenosine A_{2B} receptor: role in ligand binding and receptor function. *Biochem. Pharmacol.* **82**, 389–99 (2011).

20. Yang, X. *et al.* A covalent antagonist for the human adenosine A_{2A} receptor. *Purinergic Signal.* **13**, 191–201 (2017).

21. Cheng, Y.-C. & Prusoff, W. H. Relationship between the inhibition constant (KI) and the concentration of inhibitor which causes 50 per cent inhibition (I50) of an enzymatic reaction. *Biochem. Pharmacol.* **22**, 3099–3108 (1973).

22. Liu, W. *et al.* Structural basis for allosteric regulation of GPCRs by sodium ions. *Science.* **337**, 232–236 (2012).

23. Rodríguez, D., Piñeiro, Á. & Gutiérrez-de-Terán, H. Molecular dynamics simulations reveal insights into key structural elements of adenosine receptors. *Biochemistry* **50**, 4194–208 (2011).

24. Hess, B., Kutzner, C., van der Spoel, D. & Lindahl, E. GROMACS 4: algorithms for highly efficient, load-balanced, and scalable molecular simulation. *J. Chem. Theory Comput.* **4**, 435–447 (2008).

25. Kaminski, G. A., Friesner, R. A., Tirado-Rives, J. & Jorgensen, W. L. Evaluation and reparametrization of the OPLS-AA force field for proteins via comparison with accurate quantum chemical calculations on peptides. *J. Phys. Chem. B* **105**, 6474–6487 (2001).

26. Berger, O., Edholm, O. & Jähnig, F. Molecular dynamics simulations of a fluid bilayer of dipalmitoylphosphatidylcholine at full hydration, constant pressure, and constant temperature. *Biophys. J.* **72**, 2002–2013 (1997).

27. Marelius, J., Kolmodin, K., Feierberg, I., Åqvist, J. & Aqvist, J. Q: a molecular dynamics program for free energy calculations and empirical valence bond simulations in biomolecular systems. *J. Mol. Graph. Model.* **16**, 213–225 (1998).

28. Jespers, W., Esguerra, M., Åqvist, J. & Gutiérrez-de-Terán, H. QligFEP: an automated workflow for small molecule free energy calculations in Q. *J. Cheminform.* **11**, 26 (2019).

29. King, G. & Warshel, A. A surface constrained all-atom solvent model for effective simulations of polar solutions. *J. Chem. Phys.* **91**, 3647–3661 (1989).

30. Lee, F. S. & Warshel, A. A local reaction field method for fast evaluation of long-range electrostatic interactions in molecular simulations. *J. Chem. Phys.* **97**, 3100–3107 (1992).

31. Ryckaert, J.-P., Ciccotti, G. & Berendsen, H. J. . Numerical integration of the cartesian equations of motion of a system with constraints: molecular dynamics of n-alkanes. *J. Comput. Phys.* **23**, 327–341 (1977).

32. Robertson, M. J., Tirado-Rives, J. & Jorgensen, W. L. Improved peptide and protein torsional energetics with the OPLS-AA force field. *J. Chem. Theory Comput.* **11**, 3499–3509 (2015).

33. Jespers, W. *et al.* QresFEP: an automated protocol for free energy calculations of protein mutations in Q. *J. Chem. Theory Comput.* **15**, 5461–5473 (2019).

34. Bennett, C. H. Efficient estimation of free energy differences from Monte Carlo data. *J. Comput. Phys.* **22**, 245–268 (1976).

35. Lacotte, P., Buisson, D. A. & Ambroise, Y. Synthesis, evaluation and absolute configuration assignment of novel dihydropyrimidin-2-ones as picomolar sodium iodide symporter inhibitors. *Eur. J. Med. Chem.* **62**, 722–727 (2013).

36. Krenn, W., Verdino, P., Uray, G., Faber, K. & Kappe, C. O. Determination of absolute configuration in 4-aryl-3, 4-dihydro-2(1H)-pyrimidones by high performance liquid chromatography and CD spectroscopy. *Chirality* **11**, 659–662 (1999).

37. Uray, G., Verdino, P., Belaj, F., Kappe, C. O. & Fabian, W. M. F. Absolute configuration in 4-alkyl- and 4-aryl-3,4-dihydro-2(1H)-pyrimidones: a combined theoretical and experimental investigation. *J. Org. Chem.* **66**, 6685–6694 (2001).

38. Jaakola, V. P. *et al.* Ligand binding and subtype selectivity of the human A_{2A} adenosine receptor: identification and characterization of essential amino acid residues. *J. Biol. Chem.* **285**, 13032–13044 (2010).

39. Thimm, D. *et al.* Ligand-Specific Binding and Activation of the Human Adenosine A_{2B} Receptor. *Biochemistry* **52**, 726–740 (2013).

40. Cheng, R. K. Y. *et al.* Structures of Human A_1 and A_{2A} Adenosine Receptors with Xanthines Reveal Determinants of Selectivity. *Structure* **25**, 1275-1285.e4 (2017).

41. Jespers, W. *et al.* X-Ray Crystallography and Free Energy Calculations Reveal the Binding Mechanism of A_{2A} Adenosine Receptor Antagonists. *Angew. Chemie Int. Ed.* **59**, 16536–16543 (2020).

42. Keränen, H., Gutiérrez-de-Terán, H. & Åqvist, J. Structural and energetic effects of A_{2A} adenosine receptor mutations on agonist and antagonist binding. *PLoS One* **9**, e108492 (2014).

43. Keränen, H., Åqvist, J. & Gutiérrez-De-Terán, H. Free energy calculations of A_{2A} adenosine receptor mutation effects on agonist binding. *Chem. Commun.* **51**, 3522–3525 (2015).

44. *The PyMOL Molecular Graphics System, Version 2.0.* Schrödinger, LLC.

Supplementary Information
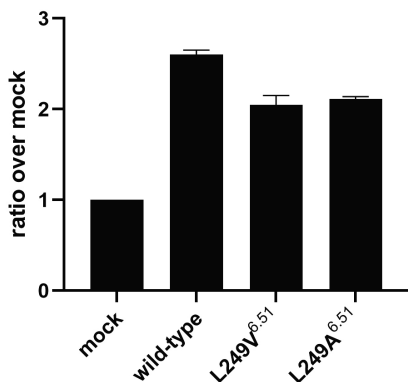
Supplementary Figure S1. Expression level of the transiently transfected WT A$_{2A}$AR, and L249V[6.51] and L249A[6.51] mutant A$_{2A}$AR at the surface of HEK293 cells. Data are shown as the mean ± SEM of three individual experiments performed in sextuplicate.
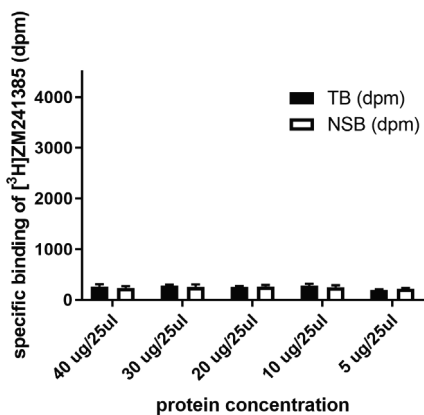
Supplementary Figure S2. Window check of HEK293 cell membrane transiently transfected by the L249[6.51]A mutant A$_{2A}$AR in the presence of 1.7 nM [^{3}H]ZM241385 in the absence (total binding; TB) and presence (non-specific binding; NSB) of NECA (100 µM). Data is shown as the mean ± SEM of three individual experiments performed in duplicate.

Supplementary Table S1. X-ray diffractometry experimental details of crystallographic (*R*)-ISAM-140 and (*S*)-ISAM-140.

Crystal data		(*R*)-ISAM140		(*S*)-ISAM140		
CCDC		1966312		1966450		
Chemical formula		$C_{19}H_{19}N_3O_3$		$C_{19}H_{19}N_3O_3$		
M_r		337.37		337.37		
Crystal system		Monoclinic		Monoclinic		
Space group		C2		C2		
Temperature (K)		100		100		
a (Å)		16,4552 (9)		16.4553 (4)		
B (Å)		8.0613 (4)		8.0605 (2)		
c (Å)		13.5259 (7)		13.5260 (3)		
α (°)		90		90		
β (°)		112.684 (3)		112.678 (1)		
γ (°)		90		90		
V (Å³)		1655.42 (16)		1655.35 (7)		
Z		4		4		
Radiation type		Cu-Kα		Cu-Kα		
μ (mm⁻¹)		0.76		0.76		
Crystal size (mm)		0.12 × 0.11 × 0.10		0.11 ×	0.01 ×	0.03
Tmin, Tmax		0.852, 0.929		-		
(sin θ/λ) max (Å⁻¹)		0.633		0.625		
Measured/Independent/ observed [I>2σ(I)] reflection		20568/3488/3266		17353/3370/3346		
Rint		0.068		0.076		
$R[F^2>2σ(F^2)]$,*wR*(F2), *S*		0.043, 0.102, 1.10		0.025, 0.069, 1.01		
Δρmax/**Δρ**min (eÅ⁻³)		0.19, −0.25		0.16, -0.20		
Absolute structure (Flack)		-0.1(2)		-0.02 (4)		

Supplementary Table S2. Experimental and FEP calculated energies for the L6.51V mutation, with the value for each FEP leg in the thermodynamic cycle included. The DDG values values are plotted on Fig 5 on the main text.

	ΔΔGexp	error	ΔΔGcalc	sem	ΔGholo	sem	ΔGapo	sem
ISAM-140(R)	-0.70	0.06	-0.39	0.36	-4.52	0.24	-4.91	0.27
ISAM-140(S)	-0.56	0.05	-0.50	0.35	-4.41	0.22	-4.91	0.28
ZM241385	0.57	0.11	0.20	0.42	-5.11	0.31	-4.91	0.29

(D)DG values and expressed in Kcal·mol⁻¹. Standard erorr of the mean (sem) calculated from 10 replica simulations (FEP) or from the experimental data (see main text). DDGexp = $-RTln(K_i^{wt}/K_i^{mut})$

Spectroscopic and analytical data for racemates and enantiomers isolated through chiral HPLC

(±) Isopropyl 4-(furan-2-yl)-2-methyl-1,4-dihydrobenzo[4,5]imidazo[1,2-*a*]pyrimidine-3-carboxylate [(±) ISAM-140][1]. ¹H NMR (300 MHz, DMSO-*d₆*), δ (ppm): 10.78 (brs, 1H), 7.67−7.23 (m, 3H), 7.19−6.84 (m, 2H), 6.52 (s, 1H), 6.44 (d, *J* = 3.3 Hz, 1H), 6.37−6.23 (m, 1H), 4.86 (h, *J* = 6.3 Hz, 1H), 2.44 (s, 3H), 1.21 (d, *J* = 6.2 Hz, 3H), 1.05 (d, *J* = 6.1 Hz, 3H). ¹³C NMR (75 MHz, DMSO-*d₆*), δ (ppm): 165.0, 153.3, 148.0,

146.0, 143.0, 142.6, 132.0, 122.3, 120.7, 117.2, 110.8, 110.2, 108.2, 94.9, 67.0, 49.7, 22.3, 22.0, 19.1. HRMS (ESI) m/z: calcd for $C_{19}H_{20}N_3O_3$ [M + H]$^+$: 338.1488; found: 338.7927.

Isopropyl (R)-4-(furan-2-yl)-2-methyl-1,4-dihydrobenzo[4,5]imidazo[1,2-a]pyrimidine-3-carboxylate [(R)-ISAM-140]. ^{1}H NMR (300 MHz, DMSO-d$_6$), δ (ppm): 10.76 (s, 1H), 7.41 (d, J = 11.0 Hz, 2H), 7.34 (d, J = 7.7 Hz, 1H), 7.04 (dt, J = 18.2, 7.0 Hz, 2H), 6.52 (s, 1H), 6.44 (d, J = 3.3 Hz, 1H), 6.35 − 6.27 (m, 1H), 4.87 (p, J = 6.3 Hz, 1H), 2.44 (s, 3H), 1.21 (d, J = 6.3 Hz, 3H), 1.05 (d, J = 6.4 Hz, 3H). ^{13}C NMR (75 MHz, DMSO-d$_6$), δ (ppm): 165.0, 153.3, 148.0, 146.0, 143.1, 142.6, 132.0, 122.3, 121.0, 117.2, 110.8, 110.2, 108.7, 95.0, 67.0, 49.7, 22.3, 22.1, 19.1. HRMS (APCI) *m/z* calcd for $C_{19}H_{19}N_3O_3$ [M+H]$^+$: 338.1499; found: 338.1501.

Isopropyl (R)-4-(furan-2-yl)-2-methyl-1,4-dihydrobenzo[4,5]imidazo[1,2-a]pyrimidine-3-carboxylate [(S)-ISAM-140]. ^{1}H NMR (300 MHz, DMSO-d$_6$), δ (ppm): 10.78 (s, 1H), 7.42 (d, J = 10.9 Hz, 2H), 7.35 (d, J = 7.8 Hz, 1H), 7.04 (dt, J = 18.2, 7.0 Hz, 2H), 6.54 (s, 1H), 6.44 (d, J = 3.3 Hz, 1H), 6.40 − 6.29 (m, 1H), 4.87 (p, J = 6.3 Hz, 1H), 2.44 (s, 3H), 1.21 (d, J = 6.3 Hz, 3H), 1.05 (d, J = 6.4 Hz, 3H). ^{13}C NMR (75 MHz, DMSO-d$_6$), δ (ppm): 165.0, 153.3, 148.0, 146.0, 143.0, 142.6, 132.0, 122.3, 120.7, 117.5, 110.8, 110.3, 108.4, 94.9, 67.0, 49.7, 22.3, 22.2, 19.0. HRMS (APCI) *m/z* calcd for $C_{19}H_{19}N_3O_3$ [M+H]$^+$: 338.1499; found: 338.1501.

Enzyme-linked Immunosorbent assay (ELISA)

The experiment was performed as described previously[2]. Briefly, 24 hours after transfection, cells were split into a 96-well poly-D- lysine-coated plates at a density of 10^6 cells per well. After an additional 24 h, the cells were fixed with 4% formaldehyde and blocked with 2% bovine serum albumin (BSA) (Sigma-Aldrich Chemie N.V., Zwijndrecht, The Netherlands) in Tris-buffered saline (TBS). Then, the cells were incubated with monoclonal M1-anti-FLAG antibody (1:2250) (Sigma-Aldrich Chemie N.V. Zwijndrecht, The Netherlands) in Tris-buffered saline (TBS)/1 mM CaCl$_2$ for 2 hours at room temperature (RT). Next, the antibody was removed and the cells were washed with TBS/1 mM CaCl$_2$ before adding the secondary antibody, monoclonal anti-Mouse-HRP (1:5000) (Jackson ImmunoResearch Europe Ltd., Cambridgeshire, UK) and incubating for 1 hour at RT. After removing the secondary antibody and washing the cells with TBS/1 mM CaCl$_2$, 3, 3',5,5'-tetramethyl-benzidine (TMB) was added and incubated for 5 minutes in the dark. The reaction was stopped with 1 M H$_3$PO$_4$, and absorbance was read at 450 nm using a Wallac EnVision 2104 Multilabel reader (PerkinElmer).

References

1. El Maatougui, A. *et al.* Discovery of potent and highly selective A$_{2B}$ adenosine receptor antagonist chemotypes. *J. Med. Chem.* **59**, 1967–1983 (2016).
2. Lane, J. R. *et al.* A novel nonribose agonist, LUF5834, engages residues that are distinct from those of adenosine-like ligands to activate the adenosine A$_{2a}$ receptor. *Mol. Pharmacol.* **81**, 475–487 (2012).